Pressure fields produced by single-bubble collapse near a corner

W. White [1,*] S. A. Beig [2] and E. Johnsen [1]
[1]*Department of Mechanical Engineering, University of Michigan, Ann Arbor, Michigan 48109, USA*
[2]*Continuum Dynamics Inc., 34 Lexington Avenue, Ewing Township, New Jersey 08618, USA*

(Received 16 September 2022; accepted 12 January 2023; published 6 February 2023)

Damage produced by repeated bubble collapse to neighboring rigid objects in hydraulic systems is an important consequence of cavitation. Although bubble collapse near a single wall has received significant attention in the past, few studies exist on the dynamics of bubbles collapsing near a corner, i.e., two flat rigid surfaces intersecting at a right angle. In this work we quantify the pressure fields produced by a single bubble collapsing near two perpendicular rigid walls. Using a high-order accurate shock- and interface-capturing method to solve the three-dimensional compressible Navier-Stokes equations for gas and liquid flows, we simulate the dynamics of a single bubble collapsing at different initial stand-off distances from the two walls. In contrast to a bubble collapsing near a single wall, the collapse of bubbles within a critical stand-off distance is not symmetric about the bisecting plane due to the interaction between the bubble and the second wall. The second wall affects the pressure produced during the collapse in the following ways: (i) For bubbles initially located sufficiently close to both walls, the reentrant jet produced during collapse no longer points in the direction normal to the closest wall but at an angle toward the corner, (ii) the part of the emitted shock with the highest amplitude propagates in line with the jet, and (iii) the bubble migrates in that same direction during its collapse with a dependence on the stand-off distance, consistent with predictions made using Kelvin impulse. The location of maximum pressure along the walls is measured for the different initial stand-off distances. Using acoustic arguments, we find a semiempirical relationship to predict the initial stand-off distances for which the maximum pressure occurs in the corner. We find that when the bubble is sufficiently close to equidistant from each boundary, the maximum pressure is observed in the corner due to the water-hammer and implosion shocks reflecting off the boundaries and intersecting in the corner. We also show that when bubbles are initially attached to either wall the wall pressure produced can be significantly increased compared to bubbles detached from either wall.

DOI: 10.1103/PhysRevFluids.8.023601

I. INTRODUCTION

Cavitation has long been known to cause structural damage to solids in a variety of hydrodynamic and acoustic applications [1–4]. The central problem in cavitation-induced damage is bubble collapse. In the idealized case of an infinite medium, a single initially spherical bubble collapses symmetrically [5], thereby compressing its contents until the interior pressure is sufficiently high to halt the collapse; the high pressures produced release a shock and possibly visible light [3,5–12]. When collapsing near a rigid surface, the bubble no longer maintains a spherical shape; a reentrant jet forms and impinges upon the opposite side of the bubble, generating a water-hammer shock [2,13–15]. Past simulations [16] show that the strength of this shock is greatest in the jet direction

*wjwhit@umich.edu

and decreases azimuthally; the maximum wall pressure is therefore along the axis of symmetry (i.e., the jet direction). This maximum pressure is an important predictor of damage [17].

Although there have been many experimental [2,12–15,18,19] and computational [16,20] studies of a bubble collapsing near a single rigid flat wall, the collapse of a bubble near a corner, i.e., two flat rigid surfaces intersecting at a right angle, has received far less interest. Such a geometry is common in internal and external flows comprising channels, ducts, cavities, etc., which can be represented by an infinite corner when the bubble is small compared to the geometry [21]. The collapse of a bubble near a corner was first investigated experimentally by [22]. Using lasers to induce cavitation bubbles and high-speed cameras to capture their dynamics, several collapse parameters were characterized. In particular, the angle of the jet and the bubble translation were measured. The work of Cui *et al.* [23] demonstrated that the bubble is primarily influenced by the nearer of the two walls. An analytical estimate for the jet angle using potential flow was proposed in [24] and it was shown through experiments that the jet angle can be accurately predicted by potential flow [25]. In simulations based on potential flow theory (e.g., boundary integral or element methods) it was found that the bubble migration toward the near wall decreases with initial stand-off distance and that the jet velocity decreases as the initial stand-off distances decrease. Additionally, the inertial collapse of a vapor bubble near slotted walls has been explored numerically and experimentally [26,27].

While accurately predicting the bubble dynamics, potential-flow-based methods cannot represent compressible-flow features such as shock waves. The pressure fields, which are essential to predicting potential damage, therefore cannot accurately be determined. Recently, shock-capturing methods have been used to investigate shock waves produced by bubbles collapsing near a wall [16,20,28,29], though these methods have yet to be applied to bubbles collapsing near a corner.

The objective of our work is to determine the time-dependent pressure fields produced by a bubble collapsing near a corner. The location and magnitude of the maximum pressure produced are not trivially determined, as the presence of the second wall deflects the direction of the reentrant jet. As a result, the strongest part of the emitted shock no longer impinges upon the closest wall surface at the projected bubble center on that wall, by contrast to collapse near a single wall. Using a high-order shock- and interface-capturing method, we simulate the collapse initially located at different stand-off distances from the two walls making up the corner. In addition to characterizing the collapse dynamics, we develop a geometric prediction of initial stand-off distances for which the maximum wall pressure occurs in the corner. The article is organized as follows. After a description of the problem and methods in Sec. II, the dynamics of a detached bubble collapsing in a corner are investigated in Sec. III. We compare our simulations to experimental results and further explore the kinematics in Sec. III C. The wall pressure and temperature produced are analyzed in Secs. III D and III E, respectively. Then the dynamics of a bubble initially attached to the wall are discussed in Sec. IV. Concluding remarks are provided in Sec. V.

II. PROBLEM DESCRIPTION AND PHYSICAL MODEL

We examine the classical Rayleigh collapse [5] of an isolated bubble near two perpendicular rigid boundaries. We assume that the bubble is initially spherical with radius $R_o = 500$ μm, filled with noncondensible gas with water vapor properties. While in practice the bubble may not be perfectly spherical and stationary at maximum expansion, experimental images show a high degree of radial symmetry at the corresponding time and we assume any interfacial velocity is small [22,24]. Initially, the water temperature T_∞ and the bubble temperature $T_{b,o}$ are 300 K. The initial gas pressure is set to 3.55 kPa, which is the saturation pressure of water at this temperature. The problem is initiated by instantaneously raising the liquid pressure $p_\infty = 3.55$ kPa by Δp. We set $\Delta p/p_\infty = 1400$ for all simulations, which is relevant to a variety of cavitation applications [30]. As illustrated in Fig. 1, the bubble is initially located a distance H_x from a vertical rigid wall in the y-z plane and a distance H_z from a horizontal rigid wall in the x-y plane. The corresponding normalized initial stand-off distances are $\delta_x = H_x/R_o$ and $\delta_z = H_z/R_o$. As in [22], the angle between the line

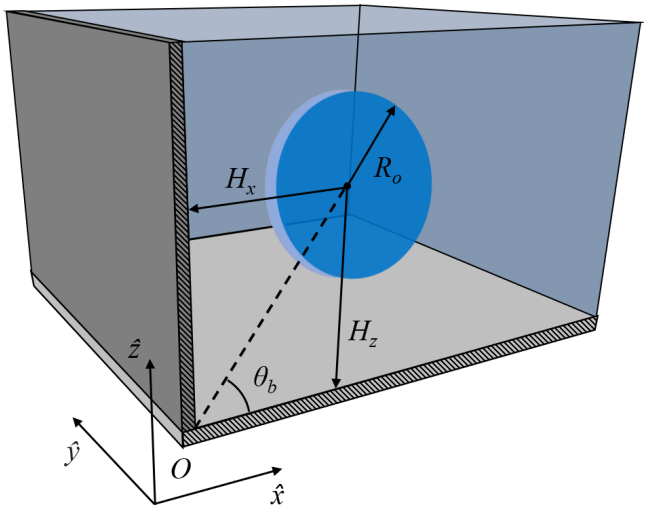

FIG. 1. Schematic of the Rayleigh collapse of a single bubble near two perpendicular rigid walls.

connecting the corner and the bubble center with the x axis is θ_b. Cases bisected by $\theta_b = \pi/4$ are symmetric about the bisecting plane. Cases in which $\delta_x > 1$ and $\delta_z > 1$ represent a bubble initially detached from both walls; $\delta_x \leqslant 1$ and/or $\delta_z \leqslant 1$ represent a bubble initially attached to both walls; $\delta_x \leqslant 1$ and $\delta_z > 1$ represent a bubble initially attached to only the y-z wall. For attached bubbles, the gas is in direct contact with the wall surface, i.e., there is no liquid film between the bubble and the wall; the initial bubble volume is adjusted such that the initial potential energy of the collapse $E_o = \Delta p V_o$ is the same as that in the detached cases. We also consider the limit of $\delta_x \to \infty$.

The compressible Navier-Stokes equations are solved in both the liquid and the gas,

$$\frac{\partial \rho}{\partial t} + \frac{\partial}{\partial x_j}(\rho u_j) = 0, \tag{1a}$$

$$\frac{\partial (\rho u_i)}{\partial t} + \frac{\partial}{\partial x_j}(\rho u_i u_j + p\delta_{ij}) = \frac{\partial \tau_{ij}}{\partial x_j}, \tag{1b}$$

$$\frac{\partial E}{\partial t} + \frac{\partial}{\partial x_j}[u_j(E+p)] = \frac{\partial}{\partial x_j}(u_i \tau_{ij} - Q_j), \tag{1c}$$

where ρ is the density, u_i the velocity vector, p the pressure, $E = \rho e + \rho u_i u_i/2$ the total energy, e the internal energy, and δ_{ij} the identity tensor. The viscous stress tensor τ_{ij} and heat flux Q_j are given by

$$\tau_{ij} = \mu\left(\frac{\partial u_i}{\partial x_j} + \frac{\partial u_j}{\partial x_i} - \frac{2}{3}\frac{\partial u_k}{\partial x_k}\delta_{ij}\right) + \mu_B \frac{\partial u_k}{\partial x_k}\delta_{ij}, \quad Q_j = -\kappa \frac{\partial T}{\partial x_j}, \tag{2}$$

where μ is the dynamic shear viscosity, μ_B is the bulk viscosity, and κ is the thermal conductivity. To capture material interfaces between different phases, we use the five-equation multiphase model [31] and solve the transport equations

$$\frac{\partial (\rho^{(k)}\alpha^{(k)})}{\partial t} + \frac{\partial}{\partial x_j}(\rho^{(k)}\alpha^{(k)} u_j) = 0, \tag{3a}$$

$$\frac{\partial \alpha^{(k)}}{\partial t} + u_j \frac{\partial \alpha^{(k)}}{\partial x_j} - \alpha^{(k)}\alpha^{(k')} \frac{\rho^{(k')}(a^{(k')})^2 - \rho^{(k)}(a^{(k)})^2}{\alpha^{(k)}\rho^{(k')}(a^{(k')})^2 + \alpha^{(k')}\rho^{(k)}(a^{(k)})^2} \frac{\partial u_j}{\partial x_j} = 0, \tag{3b}$$

TABLE I. Relevant gas and liquid properties.

Coefficients	Water vapor	Water
μ (Pa s)	1.8531×10^{-5}	8.3283×10^{-4}
μ_B (Pa s)	1.1119×10^{-5}	2.5818×10^{-3}
κ (W m^{-1} K^{-1})	0.026107	0.61497
n	1.47	1.19
B (MPa)	0	702.8
b (kg m^{-3})	0	6.61×10^{-4}
c (J kg^{-1} K^{-1})	955	3610
q (J kg^{-1})	2.1×10^{6}	-1.2×10^{6}

where a is the sound speed and k and k' represent each phase $\alpha^{(k)} = 1 - \alpha^{(k')}$. As done in relevant past studies [20,32,33], we neglect surface tension and mass transfer effects since the flow is inertia dominated. The Noble-Abel stiffened-gas equation of state [34] closes the system

$$\rho(e-q) = \frac{p}{n-1}(1-\rho b) + \frac{nB}{n-1}(1-\rho b) \quad \text{(pressure-wise)} \tag{4a}$$

$$= \rho c T + B(1-\rho b) \quad \text{(temperature-wise)}, \tag{4b}$$

where q, n, b, and B are experimentally determined parameters, given in Table I. For ideal gases, $n = \gamma$ represents the specific heat ratio, $c = c_v$ is the specific heat at constant volume, and B, q, and b are zero.

The numerical method of Beig and Johnsen [28] is used to accurately and stably represent discontinuities in the flow. The solution is advanced in time with a third-order total variation diminishing Runge-Kutta scheme [35] with an adaptive step size satisfying advection and diffusion stability constraints. The spatial scheme is high-order accurate, in which a fifth-order Weighted Essentially Non-Oscillatory (WENO) scheme [36] is used at shocks and interfaces [37] and fourth-order central difference elsewhere; the sensor of Henry de Frahan [38] discriminates between these regions. For stability purposes, the source term in (3b) is set to zero for the first 1000 time steps [16] and interfaces are initially smoothed over three computational cells. The validity of this numerical scheme was thoroughly evaluated by Beig and Johnsen [28].

Owing to the problem symmetry with respect to the x-z plane, we simulate only half of the domain with a symmetry boundary condition along this plane. The walls are adiabatic and perfectly reflecting with no slip. Nonreflecting boundary conditions are used along the remaining boundaries. A uniform Cartesian grid with 192 cells per initial bubble radius is used and the largest domain size is $8R_o \times 8R_o \times 4R_o$. Beig and Johnsen [28] examined the convergence of the spherical case in comparison with the Keller-Miksis [39] solution and demonstrated that the chosen resolution is satisfactory. To understand the dependence of the bubble dynamics on the proximity of the walls, we conduct simulations in which the stand-off distances are varied as follows: $0.25 \leqslant \delta_x \leqslant 4.0$ and $0.25 \leqslant \delta_z \leqslant 4.0$. Due to the infinite nature of the walls, the dynamics of cases with initial stand-off distances $(\delta_x, \delta_z) = (a, b)$ are the same as those with initial stand-off distances $(\delta_x, \delta_z) = (b, a)$, so we only simulate cases with $\delta_z \geqslant \delta_x$. As a reference, we compare our results to bubble collapse near a single wall.

III. DETACHED BUBBLES

A. Qualitative dynamics

We start by examining the dynamics and resulting pressure fields of detached bubbles. Figures 2 and 3 show contours of (numerical) schlieren, pressure, and velocity for simulations with $(\delta_x, \delta_z) =$

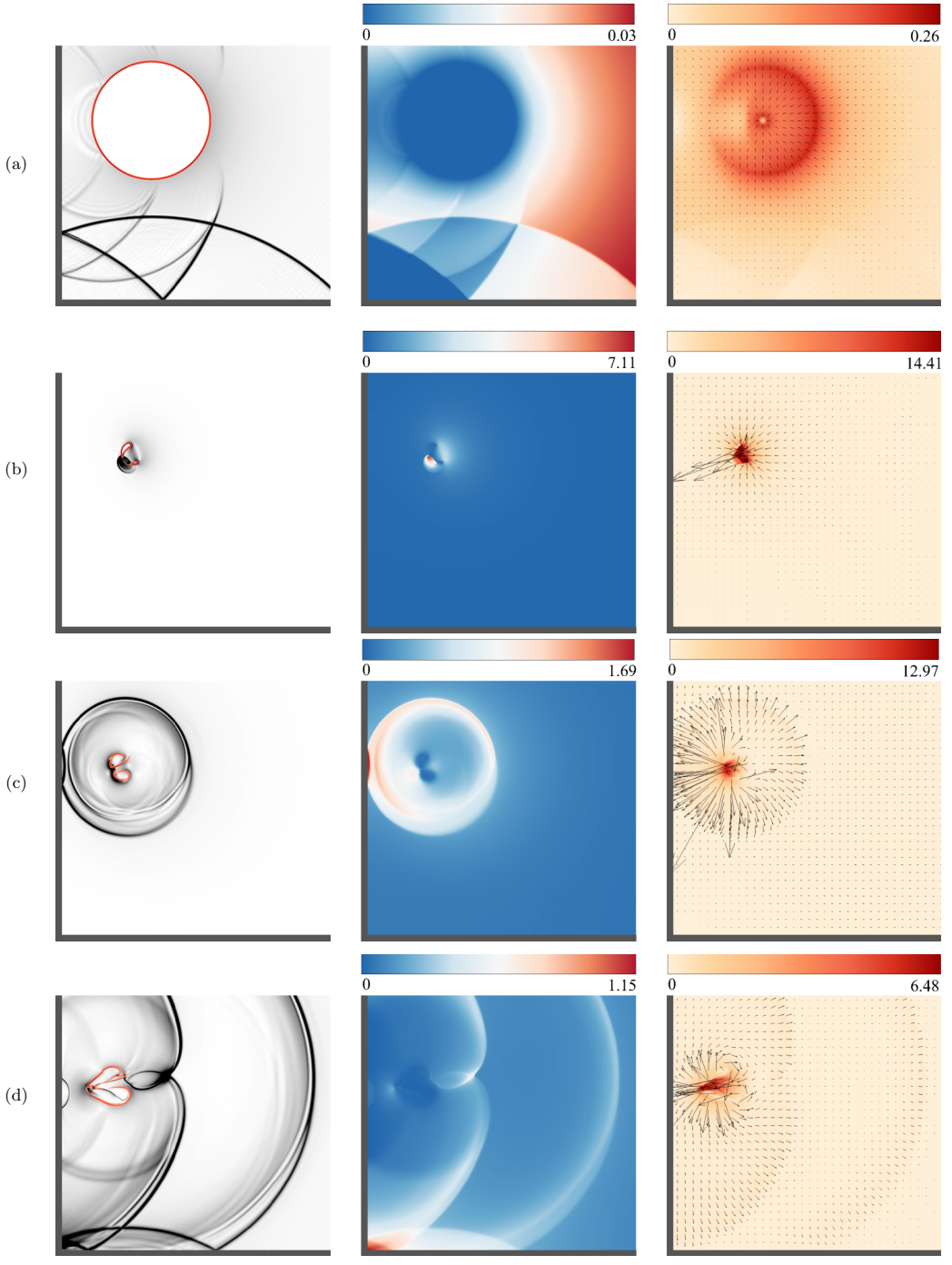

FIG. 2. Contours of (numerical) schlieren, pressure normalized by $\rho_l a_l \sqrt{\Delta p/\rho_l}$ and velocity magnitude normalized by $\sqrt{\Delta p/\rho_l}$ for $(\delta_x, \delta_z) = (1.5, 3.0)$. Contours are of times (a) $t = 0.163$, (b) $t = 1.155$, (c) $t = 1.199$, and (d) $t = 1.294$, normalized by the Rayleigh collapse time $0.915 R_0 \sqrt{\rho_l/\Delta p}$.

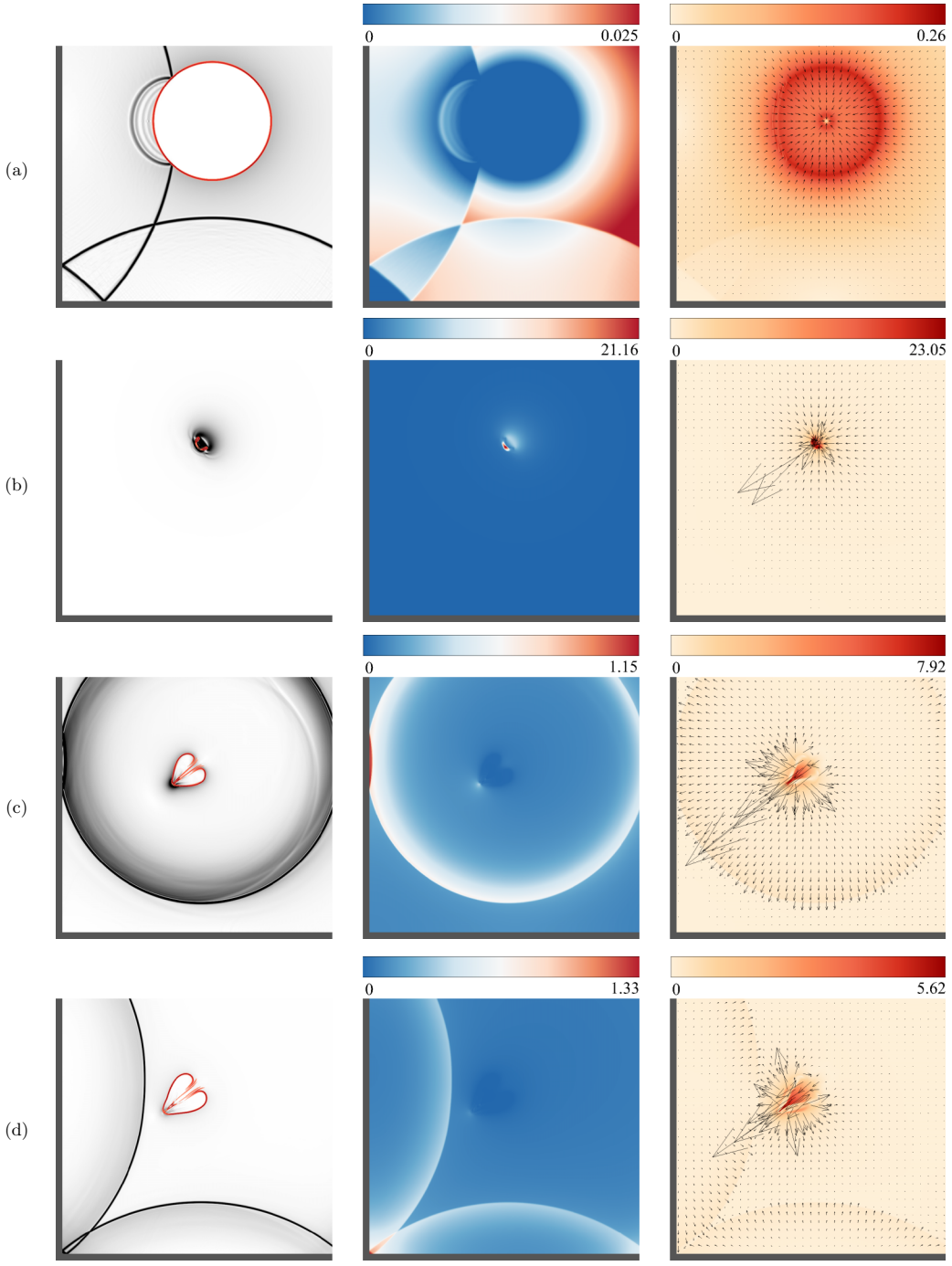

FIG. 3. Contours of (numerical) schlieren, pressure normalized by $\rho_l a_l \sqrt{\Delta p/\rho_l}$ and velocity magnitude normalized by $\sqrt{\Delta p/\rho_l}$ for $(\delta_x, \delta_z) = (2.5, 3.0)$. Contours are of times (a) $t = 0.163$, (b) $t = 1.102$, (c) $t = 1.198$, and (d) $t = 1.261$, normalized by the Rayleigh collapse time $0.915 R_0 \sqrt{\rho_l/\Delta p}$.

(1.5, 3.0) and $(\delta_x, \delta_z) = (2.5, 3.0)$, respectively. Time is normalized by the Rayleigh collapse time $t_c = 0.915R_0\sqrt{\rho_l/\Delta p}$. These two cases are chosen to contrast the dynamics that occur when $\delta_x/\delta_z \approx 1$ and when δ_x/δ_z is farther from unity. As the collapse begins, a rarefaction wave propagates outward while a transmitted shock wave converges toward the bubble center. The rarefaction wave impinges upon the closest wall first and then the farther wall. Upon each interaction, the relevant part of the wave is reflected back toward the bubble. Until the time when the reflected wave hits the bubble, the bubble is unaffected by the walls, so the collapse remains spherical [16]. The interaction of the reflected rarefactions with the bubble gives rise to a nonuniform pressure distribution around the bubble, thus causing the interface to accelerate asymmetrically. The pressure fields resulting from these wave dynamics can be understood as the effects of the image bubbles, whose influence is inversely proportional to their distance from the original bubble. However, by contrast to potential flow calculations [24] in which these effects instantaneously take place, the present simulations account for the finite propagation speed of the waves. Following early contraction, a region of high-pressure and high-speed liquid is visible on the far side of the bubble. A reentrant jet forms in a direction that is normal to neither wall and subsequently impinges upon the opposite side of the bubble. This impact generates a water-hammer shock and causes the bubble to take the shape of a vortex ring [Figs. 2(b) and 3(b)]. The water-hammer shock subsequently interacts with the bubble, thus causing it to collapse and emit another shock. The pressure of the resulting shocks varies azimuthally and appears to be highest in the direction of the jet [16].

For $(\delta_x, \delta_z) = (2.5, 3.0)$, the collapse is close to symmetric as the initial location is close the angle $\theta_b = \pi/4$. The wave front impinging upon the closer wall interacts with the bubble slightly before the wave front impinging upon the farther wall. This small difference in time between the two wave fronts gives rise to an asymmetry that is visible only at late times in the collapse. Though not shown here, a bubble initially located along the bisection plane exhibits symmetry in its collapse. For the case with $(\delta_x, \delta_z) = (1.5, 3.0)$, the nonuniformity of the collapse is clear, particularly at the point of the jet impact impacting the bubble wall and late times.

The topology of the bubble throughout the collapse varies significantly with different initial stand-off distances, which dictate the jet direction. For $(\delta_x, \delta_z) = (2.5, 3.0)$, the upper and lower portions of the bubble at the point of jet impact are visibly very similar, whereas for $(\delta_x, \delta_z) = (1.5, 3.0)$ the upper region of the bubble is noticeably larger. Also different between these two cases are the shock waves that intersect in the corner. For the case with $(\delta_x, \delta_z) = (1.5, 3.0)$, the water-hammer and implosion shocks are distinct when they intersect in the corner. The substantial distance from the corner in the case with $(\delta_x, \delta_z) = (2.5, 3.0)$ results in a single shock by the time it impinges upon the walls. When the ratio δ_x/δ_z is small or large the dynamics of the collapse are more similar to those near a single wall. For cases where $\delta_x \approx \delta_z$, the reflected waves intersect the bubble at the same time and the collapse is symmetric about $\theta_b = \pi/4$. The observed bubble shapes match well with those from experimental studies, and the use of simulations in the present work affords the ability to examine the kinematics of the collapse in detail and to quantify the pressure and temperature fields.

B. Characterization of the bubble nonspherical shape

For bubbles lying off the bisecting plane, spherical symmetry is broken when the first portion of the reflected rarefaction front interacts with the bubble. Bubbles sufficiently far from the walls, i.e., distances such that the instant of collapse (minimum volume) occurs before the time when the reflected rarefaction interacts again with the bubble, remain spherical until collapse. Comparing this time of flight with the collapse time, it follows that bubbles within the following stand-off distance from either wall collapse nonspherically:

$$\delta_{cr} \approx 0.5\left[1 + \sqrt{\frac{\rho_l a_l^2}{\Delta p}} + \left(\frac{p_\infty}{(\gamma-1)\Delta p}\right)^{1/3(\gamma-1)}\right]. \tag{5}$$

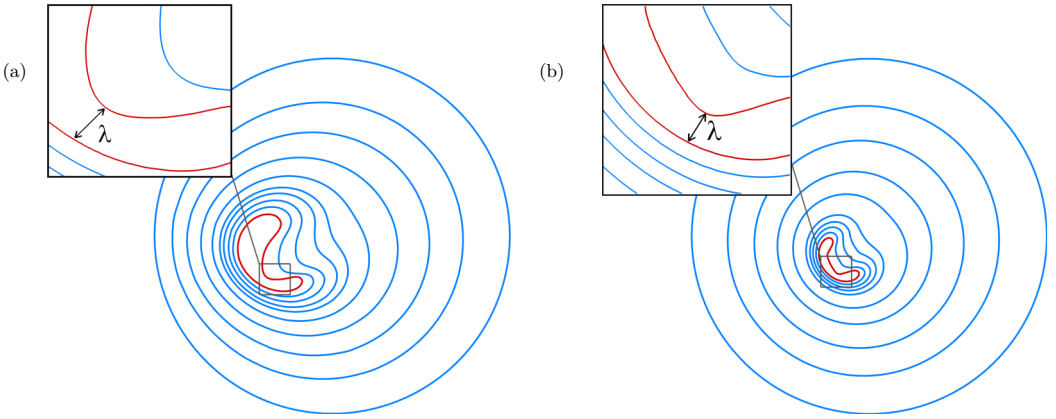

FIG. 4. Outlines for (a) $(\delta_x, \delta_z) = (1.5, 3.0)$ and (b) $(\delta_x, \delta_z) = (2.5, 3.0)$ and the measurement of λ.

This yields $\delta_{cr} \approx 10.5$ for the driving pressure used here. All simulations, with the exception of single-wall cases for comparison, have both δ_x and δ_z smaller than δ_{cr} and as such the dynamics are affected by both walls.

The collapse properties are characterized by the two geometric parameters δ_x and δ_z for certain geometrical properties (e.g., jet angle and migration angle) over a range of initial stand-off distances. Other quantities however depend on the absolute distance from the walls; e.g., the bubble reaches a smaller volume before the reflected rarefaction waves can return and inform the bubble of the geometry. As such, the characterization of quantities associated with the interfacial velocity (collapse time, jet speed, etc.) require additional information beyond the ratio δ_x/δ_z. For this purpose we calculate the deviation from the spherical shape of the bubble $\xi = \pi\lambda/\mathcal{P}$, where λ is the film thickness and $\mathcal{P}$ is the perimeter of the bubble's outline along the center plane. The film thickness is the shortest distance between the front and back sides of the bubble at any given time, as illustrated in Fig. 4. In the limit of a spherical collapse $\lambda = 2R(t)$ and $\xi = 1$ at all times during the collapse. When the jet forms, the shortest distance between the front and back sides is at the tip of the jet. The area of the bubble cross section in this case is always greater than that of a circle with diameter equal to the film thickness, so for nonspherical collapse $0 \leqslant \xi \leqslant 1$. For all bubbles that are initially spherical, the film thickness decreases from $2R_0$ at $t = 0$ to zero at the point at which the jet impinges the opposite side; we calculate the film thickness and perimeter of the bubble along the center plane until this point in time.

To appreciate the nonspherical evolution of the bubble, outlines of the interface along the center plane up to the point at which $\lambda \approx 0.05$ are shown in Fig. 4 for $(\delta_x, \delta_z) = (1.5, 3.0)$ and $(\delta_x, \delta_z) = (2.5, 3.0)$. Figure 5 shows ξ for different initial stand-off distances with λ chosen to be around 0.05, as at this value the jet has nearly penetrated the bubble wall. A different value of λ close to zero may be chosen to calculate ξ; however, the resultant trend in ξ will be similar, just scaled. The collapse is most nonspherical for the bubbles closest to the wall, as evidenced by values of ξ close to zero. As expected from the geometry, the values of ξ are symmetric about the line $\delta_x = \delta_z$. The data nearly collapse onto a single line when plotted versus $\min(\delta_x, \delta_z)$, indicating the closest wall has the greatest effect on the collapse. The more spherical collapses occur farthest from the corner where the walls have the least effect. The strength of the initial rarefaction is inversely proportional to its original distance from the bubble, so increasing δ_x or δ_z decreases its effect on the collapse. For two cases with the same values of δ_x/δ_z, the case with the greater value of $\sqrt{\delta_x^2 + \delta_z^2}$ collapses more spherically for the same reason. The strength of all subsequent waves that interact between the bubble and the walls decreases in magnitude while still contributing to the asymmetric collapse by modifying the driving pressure and acceleration of the interface. When $\delta_x \neq \delta_z$, the nonspherical dynamics are most affected by the waves reflected off the closest wall, until the wave reflected off

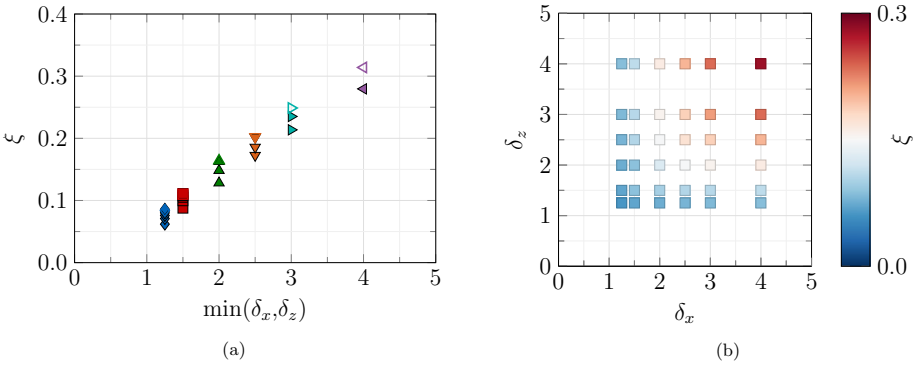

FIG. 5. Nonsphericity ξ vs (a) $\min(\delta_x, \delta_z)$ and (b) initial stand-off distances. Blue diamonds denote $\delta_x = 1.25$, red squares $\delta_x = 1.5$, green deltas $\delta_x = 2.0$, orange gradients $\delta_x = 2.5$, teal right triangles $\delta_x = 3.0$, and purple left triangles $\delta_x = 4.0$. Corner cases are closed and single-wall cases are open.

the other wall returns. At this point, the collapse becomes more nonspherical due to the enhanced interactions of the additional sinks. The dynamics of two bubbles with the same values of δ_x/δ_z, but different values of δ_x and δ_z are distinct because of the different reflected rarefaction strengths and because the bubble-wave interactions begin at different points in the collapses. Those bubbles initially closest to the corner experience the least spherical collapses because the asymmetry is imparted on the bubble interface earliest in the collapse. For a given δ_x, increasing δ_z decreases the deviation from spherical shape until the point at which $\delta_z > \delta_{cr}$, in which case the dynamics are those of a bubble near a single wall, as the rarefaction reflected off the additional wall does not reach the bubble before it collapses.

The increased nonsphericity due to the bubble-wall interactions affects key collapse quantities. The minimum volume $V_{\min}$ and collapse time t_{collapse} (time to minimum volume) are shown in Figs. 6 and 7, respectively, for different initial stand-off distances. The minimum bubble volume is a measure of the strength of the emitted shock; a smaller minimum volume gives rise to a higher bubble pressure and thus stronger emitted shock. Holding either stand-off distance constant and increasing the other leads to a smaller minimum volume. This behavior is consistent with collapse near a single wall, where the minimum volume achieved at collapse is smaller for bubbles increasingly far from the wall, because their collapse is more spherical. As with ξ the data collapse

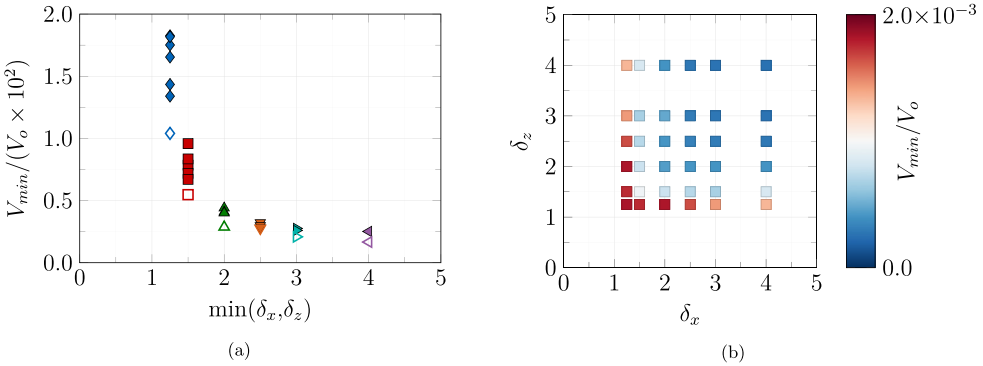

FIG. 6. Minimum volumes vs (a) $\min(\delta_x, \delta_z)$ and (b) initial stand-off distances. Blue diamonds denote $\delta_x = 1.25$, red squares $\delta_x = 1.5$, green deltas $\delta_x = 2.0$, orange gradients $\delta_x = 2.5$, teal right triangles $\delta_x = 3.0$, and purple left triangles $\delta_x = 4.0$. Corner cases are closed and single-wall cases are open.

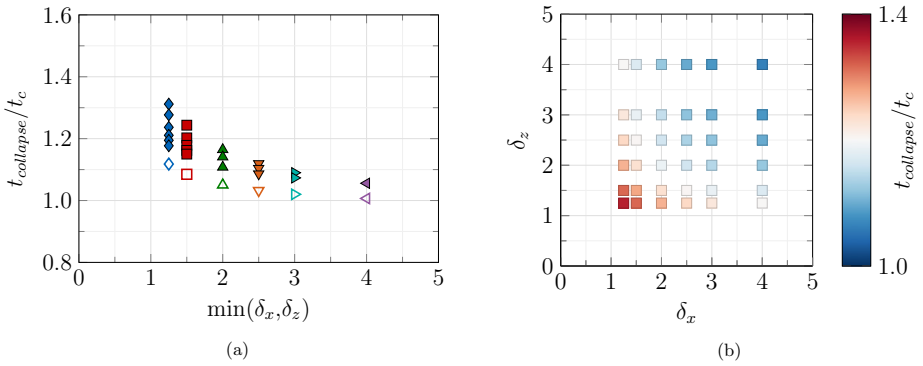

FIG. 7. Collapse times scaled by the Rayleigh collapse time vs (a) $\min(\delta_x, \delta_z)$ and (b) initial stand-off distances. Blue diamonds denote $\delta_x = 1.25$, red squares $\delta_x = 1.5$, green deltas $\delta_x = 2.0$, orange gradients $\delta_x = 2.5$, teal right triangles $\delta_x = 3.0$, purple left triangles $\delta_x = 4.0$, and gray circles other single-wall cases. Corner cases are closed and single-wall cases are open.

when $V_{\min}$ is plotted against $\min(\delta_x, \delta_z)$. For a given δ_x however, the minimum volume is larger in the cases near a corner than those near a single wall. These larger minimum volumes can be explained by the dynamics leading to more intricate bubble morphologies of the collapses when compared to those near a single wall, which results in less effective focusing of the liquid kinetic energy. The impact of this decreased focus can also be seen in the longer collapse times for bubbles near a corner than those in collapse near a single wall. The increased collapse time is a consequence of the two additional image sinks, whose induced velocity reduces the inward interfacial velocity. Bubbles initially closest to the wall have the longest collapse times because the initially emitted rarefaction wave reduces the local driving pressure sooner in the collapse than in the case of bubbles located farther away from the wall; a lower driving pressure slows down the dynamics and thus give rise to a longer collapse time [5]. Under the influence of both walls making up the corner, this effect is increased as the second wall reflects an additional portion of the initial rarefaction wave that then returns to the bubble and further decreases the pressure field, although to a lesser degree than the portion of the wave that returns from the closest wall. This behavior is supported by the observation that bubbles collapsing near a corner have longer collapse times than a bubble collapsing near a single wall. For all cases near the corner, the collapse time is notably longer than the Rayleigh collapse time for these reasons.

C. Bubble kinematics and dynamics

The kinematics and dynamics of bubbles collapsing near a corner have been the focus of past experimental studies [22–24], so we use this section to validate our results and examine specific features of the collapse. As illustrated in Figs. 2 and 3, the direction of the reentrant jet formed in bubble collapse near a corner is dependent on the initial stand-off distances from the two walls; additionally, the part of the emitted shock with the highest amplitude appears to propagate in the direction of the jet. In cases where the bubble is sufficiently far from the second wall ($\delta_z > \delta_{cr}$), the jet is perpendicular to the closest wall. However, for bubbles sufficiently close to both walls [$(\delta_x, \delta_z) < \delta_{cr}$], the jet points in a direction that is not at the closest initial location along either wall, but somewhere in between, which is one of the ways in which the shock wave dynamics are affected by the presence of the second wall.

To calculate the jet angle, we define the jet tip as the point along the interface on the far side of the bubble that is closest to the interface on the far side, once the bubble starts to involute, i.e., is no longer purely concave. The jet angle as a function of time is then calculated as the angle between jet positions at successive time steps. The jet angle is averaged over the interval starting from the time

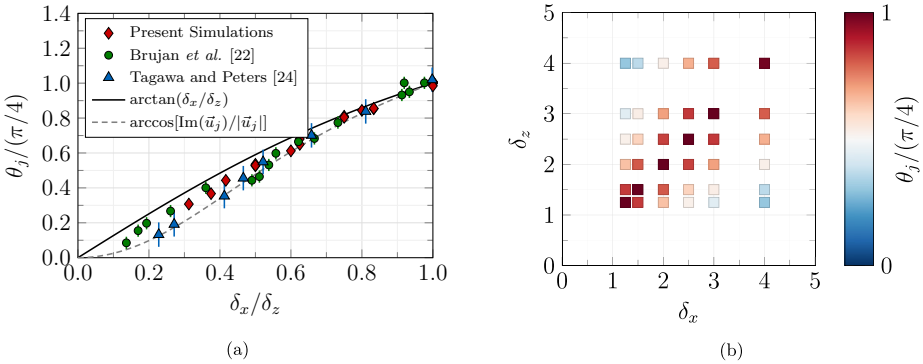

FIG. 8. Jet angle θ_j as a function of (a) the ratio of the initial stand-off distances δ_x/δ_z, with red diamonds denoting direct simulations, green circles experimental data from [22], blue triangles experimental data from [24], black line [$\arctan(\delta_x/\delta_z)$] Eq. (6), and gray dashed line ($\arccos[\mathrm{Im}(\vec{u}_j)/|\vec{u}_j|]$) Eq. (8), and (b) initial stand-off distances, with blue diamonds denoting $\delta_x = 1.25$, red squares $\delta_x = 1.5$, green deltas $\delta_x = 2.0$, orange gradients $\delta_x = 2.5$, teal right triangles $\delta_x = 3.0$, purple left triangles $\delta_x = 4.0$, and gray circles other single-wall cases. Corner cases are closed and single-wall cases are open.

at which the jet is first detected and the time at which the jet impacts the far side of the bubble; the angle is nearly constant throughout this interval. For a range of initial stand-off distances similar to ours, experimental data were found to obey the power law [22]

$$\theta_j = \frac{\pi}{2}(\delta_x/\delta_z)^m \approx \arctan(\delta_x/\delta_z), \quad m = 0.981 \pm 0.035, \tag{6}$$

where m is a parameter fit to experimental results. Another measure of jet angle is from Tagawa and Peters [24], who used potential flow to determine the jet angle based on the jet velocity $\vec{u}_j$,

$$\frac{\vec{u}_j}{C} = \frac{e^{i\theta_b} - e^{i(2\pi-\theta_b)}}{[1-\cos(2\theta_b)]^{3/2}} + \sum_{k=1}^{g-1}\left(\frac{e^{i\theta_b} - e^{i(2\pi k/g-\theta_b)}}{[1-\cos(2\theta_b - 2\pi k/g)]^{3/2}} + \frac{e^{i\theta_b} - e^{i(2\pi k/g+\theta_b)}}{[1-\cos(2\pi k/g)]^{3/2}}\right), \tag{7}$$

where $C = p/(\pi\sqrt{128}R_0^2)$, g is the integer index of the corner geometry, p is the sink strength, and $g = 2$ describes two perpendicular walls. From Eq. (7) the jet angle is

$$\theta_j = \arccos[\mathrm{Im}(\vec{u}_j)/|\vec{u}_j|]. \tag{8}$$

Figure 8 shows the jet angle as a function of δ_x/δ_z, comparing our numerical simulations to the experimental data from [22,24], as well as to theoretical results from Eqs. (6) and (8). Our simulation results fit well within the bounds of the error bars of Brujan *et al.* [22] and Tagawa and Peters [24] and follow trends similar to those proposed in each, respectively. For most of the δ_x/δ_z range under consideration, the models provide upper and lower bounds to the experimental and simulations data. This agreement indicates that our simulations also accurate represent the jet dynamics governed by interactions between the bubble and its images as described by potential flow theory.

Over the course of the collapse, the bubble migrates toward both walls to varying degrees. We calculate the volumetric centroid of the bubble by taking moments of the volume fraction field, throughout the collapse. Bubbles with one of δ_x or δ_z greater than δ_{cr} follow a straight line toward the closest wall. Bubbles with initial stand-off distances such that they are affected by both walls follow trajectories somewhere in between. One method of characterizing the trajectory is utilized by Brujan *et al.* [22], who quantified the general direction of the bubble motion with a parameter defined as the migration angle θ_{mig}, measured between the initial centroid location and the location at collapse. Figure 9 compares this migration angle between our simulations, Brujan's experiments, and Eqs. (6) and (8). Again, the agreement between simulations and experiments is reasonable;

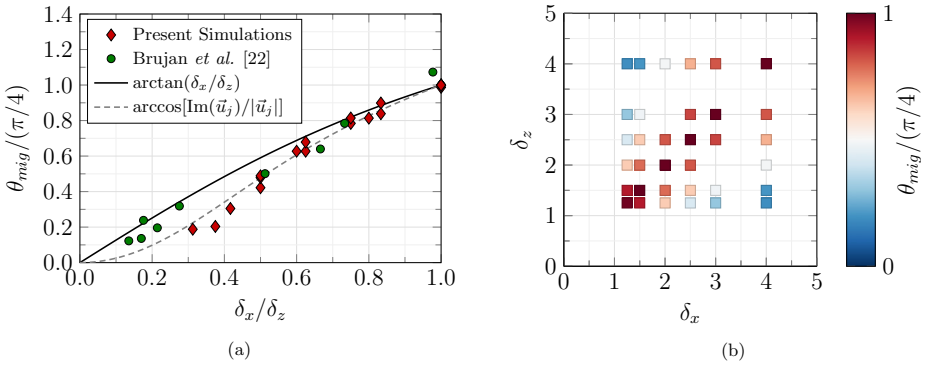

FIG. 9. Bubble migration angle θ_j as a function of (a) the ratio of the initial stand-off distances δ_x/δ_z, with red diamonds denoting direct simulations, green circles experimental data from [22], black line [$\arctan(\delta_x/\delta_z)$] Eq. (6), and gray dashed line ($\arccos[\mathrm{Im}(\vec{u}_j)/|\vec{u}_j|]$) Eq. (8), and (b) initial stand-off distances, with blue diamonds denoting $\delta_x = 1.25$, red squares $\delta_x = 1.5$, green deltas $\delta_x = 2.0$, orange gradients $\delta_x = 2.5$, teal right triangles $\delta_x = 3.0$, purple left triangles $\delta_x = 4.0$, and gray circles other single-wall cases. Corner cases are closed and single-wall cases are open.

discrepancies may be explained by the deviation in angle between the first and subsequent collapses in [22]. Our numerical simulations agree well with the potential flow model from [24], while the experiments show better agreement with Eq. (6), which was developed based on these experiments.

The location of the bubble centroid at collapse is important as it is a good approximation of the origin of the shock emitted upon collapse. Figure 10(a) shows the distance $\min(\delta_{xc}, \delta_{zc})$ between of the bubble centroid at collapse and the near wall, where δ_{xc} and δ_{zc} are the normalized x and z positions of the bubble centroid at the point of collapse.

While the centroid positions at collapse are very similar for collapse near a corner and collapse near a single wall, the latter are systematically closer to the wall than the former. The difference in centroid locations between the single wall and corner cases is largest near the corner and monotonically decreases as $\min(\delta_x, \delta_z)$ increases. In other words, the location of the bubble at collapse is slightly farther from the wall in collapse near a corner due to the effect of the second

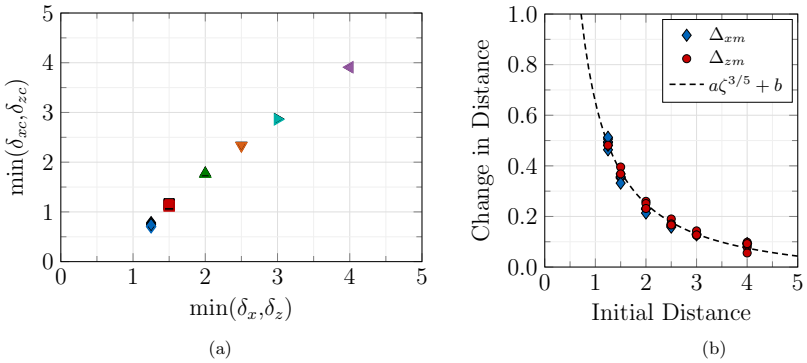

FIG. 10. (a) Plot of $\min(\delta_{xc}, \delta_{zc})$ vs $\min(\delta_x, \delta_z)$, with blue diamonds denoting $\delta_x = 1.25$, red squares $\delta_x = 1.5$, green deltas $\delta_x = 2.0$, orange gradients $\delta_x = 2.5$, teal right triangles $\delta_x = 3.0$, and purple left triangles $\delta_x = 4.0$. Corner cases are closed and single-wall cases are open. (b) Migration from initial stand-off distances to collapse location vs initial stand-off distance, with red circles denoting Δ_{xm} vs δ_x and blue squares Δ_{zm} vs δ_z. The black dashed curve is a direct fit of Δ_{xm} and Δ_{zm} to $a\zeta^{3/5} + b$, with $a \approx 1.9$ and $b \approx -0.06$.

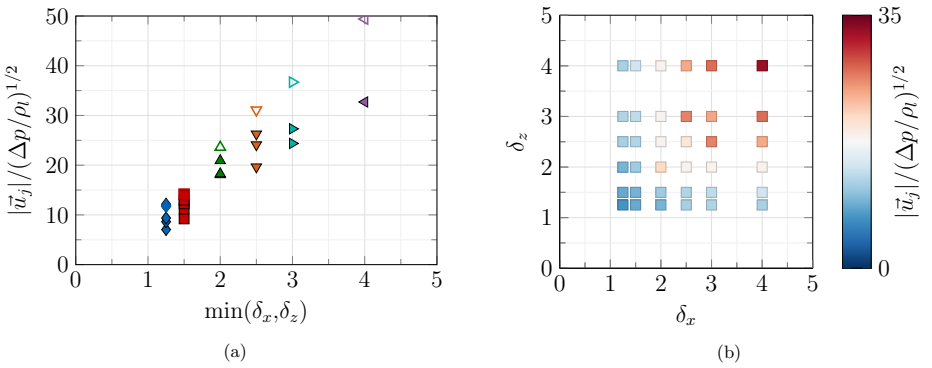

FIG. 11. Maximum jet speed vs (a) $\min(\delta_x, \delta_z)$ and (b) initial stand-off distances. Blue diamonds denote $\delta_x = 1.25$, red squares $\delta_x = 1.5$, green deltas $\delta_x = 2.0$, orange gradients $\delta_x = 2.5$, teal right triangles $\delta_x = 3.0$, and purple left triangles $\delta_x = 4.0$. Corner cases are closed and single-wall cases are open.

wall. This behavior is consistent with the trend in the maximum wall pressure observed in the next section, in that the difference between the maximum wall pressure in the single-wall and corner cases decreases with increasing $\min(\delta_x, \delta_z)$.

The distance traveled from the initial position is calculated as $(\Delta_{xm}, \Delta_{zm}) = (\delta_x - \delta_{xc}, \delta_z - \delta_{zc})$. This motion is important when predicting impact loads as the centroid location at collapse is a reasonable measure of the location where the shock is released. Figure 10(b) shows the distance traveled in each direction, measured from the initial stand-off distances to the position at collapse.

Bubbles that are initially farthest from either wall experience the smallest change in the position of their centroids until the collapse. The changes in distance in x and in z follow a similar trend. Supponen *et al.* [40] defined an anisotropy parameter $\zeta = 0.195(\delta/R_0)^{-2}$, which is a dimensionless version of the Kelvin impulse and showed that it can be used to predict the dynamics of bubbles collapsing near a single rigid wall. They further suggested that for strong jets the displacement of the centroid scales with $\zeta^{3/5}$ when the bubble location is the point where the jet impacts the opposite side ($\zeta > 0.1$ is considered strong; present simulations have $0.5856 \leqslant \zeta \leqslant 0.0572$). Our simulations exhibit a similar dependence of the migration distance on the stand-off distance, which can be seen as the fit curve in Fig. 10(b). The bubble centroid at collapse can be then predicted by $\delta_{jc} = \delta_j - a\zeta_j^{3/5} - b$, where $j = x, z$. The necessity to scale and add a constant to $\zeta^{3/5}$ is likely due to different measurements of the bubble centroids and to the effects of the second wall. With the introduction of a constant scaling and offset to account for the different physics in the corner compared to near a single wall, the Kelvin impulse accurately predicts the migration behavior observed in each direction. The motion toward both walls is a key difference in the dynamics between those of collapse near a single wall.

The speed of the jet is indicative of the strength of the water-hammer shock produced upon impact with the opposite side of the bubble, as its pressure scales as $\rho_l a_l |u_j|$, where ρ_l is the liquid density, a_l is the sound speed in the liquid, and $|u_j|$ is the velocity magnitude [41]. Figure 11 shows the maximum jet speed for different initial stand-off distances. The results are consistent with our observations of minimum volume and collapse time, with the fastest jets occurring farthest from the corner and the slowest occurring closest. Based on the observation that nonsphericity increases as bubbles start their collapse closer to the walls, the maximum jet speed by the deviation from spherical shape indicates that more spherical collapses give rise to increased speeds. Additionally, when affected by two walls, the jet speeds are not as high as those achieved in collapse near a single wall, consistent with the fact that the velocity is reduced due to the flow induced by the additional two image sources. As such, the water-hammer pressure is lower for bubble collapse near a corner than near a single wall.

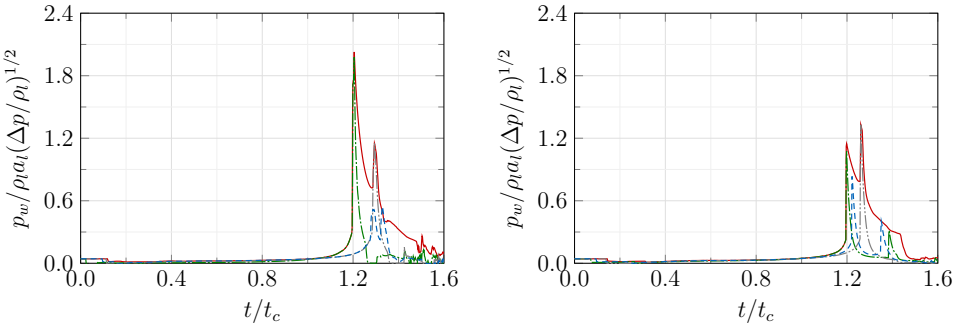

FIG. 12. Time history of wall pressure at the location of the maximum wall pressure (red solid line), at the corner (green dash-dotted line), $(x, y, z) = (\delta_x, 0, 0)$ (gray dash–double-dotted line), and $(x, y, z) = (0, 0, \delta_z)$ (blue dashed line) for (a) $(\delta_x, \delta_z) = (1.5, 3.0)$ and (b) $(\delta_x, \delta_z) = (2.5, 3.0)$.

D. Wall pressure

The maximum pressure produced by a collapsing bubble along a wall is the quantity characterizing impact loads in cavitation erosion. If only δ_x or δ_z is greater than δ_{cr}, the problem corresponds to collapse near a single wall, in which case the maximum pressure decreases with increasing initial stand-off distance [16,20]. In the present work, all cases near the corner have initial stand-off distances within δ_{cr}. Since the dynamics are affected by both walls, the pressure produced by collapse near a corner is different than that near a single wall in the following ways: (i) The maximum reentrant jet velocity is affected by the proximity of the second wall, (ii) the part of the emitted shock with the highest amplitude propagates in the direction of the jet, which no longer points toward the nearest wall but is deflected toward the corner, and (iii) the location of the bubble centroid at collapse is attracted toward the second wall. For bubbles whose collapse is affected by both walls, the maximum pressure is unlikely to be produced at the location along the wall closest to the initial bubble position, as would be the case in collapse near a single wall. To better understand these effects at play, Fig. 12 shows the time history of the wall pressure at $(x, y, z) = (\delta_x, 0, 0)$, $(x, y, z) = (0, 0, \delta_z)$, the pressure at the corner, and the maximum wall pressure over the course of the simulation, for two sets of stand-off distances. Interpreting the data in conjunction with Figs. 2 and 3, the wall pressure initially decreases due to the rarefaction reflecting off the closest wall and then does not change significantly until the water-hammer shock and implosion shock interact with the closest wall, which causes a rapid increase in the pressure. For the case $(\delta_x, \delta_z) = (1.5, 3.0)$, the maximum wall pressure is achieved by this process, though at a location along the wall closer to the corner. A similar phenomenon occurs along the farther wall, though the peak pressure is lower. The time delay between the water-hammer and implosion shocks can be seen in the first peak of Fig. 12(a), with the maximum occurring only after the implosion shock impinges upon the wall. In the case $(\delta_x, \delta_z) = (2.5, 3.0)$, the portion of the shock front reflecting off the closest wall and that reflecting off the farther wall intersect close to the corner, thereby giving rise to the highest pressure at that location, even if the shocks do not exactly intersect there. In this case, there is no delay between the water-hammer and implosion shocks in this case, as expected from Fig. 3.

The above observations suggest that there are geometrical configurations for which the pressure generated in the corner is higher than that produced along either wall. Despite the complex bubble morphologies and shock dynamics in these collapses, acoustic arguments can be used to predict the initial stand-off distances for which the maximum wall pressure is higher in the corner than along either wall. In the case of $\delta_x > \delta_{cr}$ and $\delta_z > \delta_{cr}$, the collapse is spherical and the shock pressure is

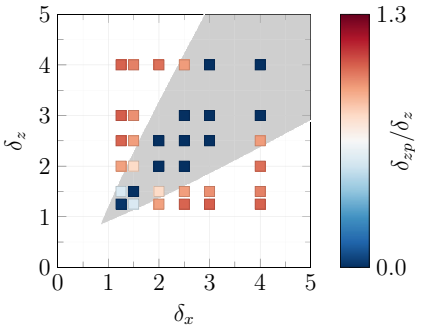

FIG. 13. Location of maximum wall pressure δ_{zp}/δ_z. The gray region shows $p_r \geqslant 1$.

given by

$$\frac{p_s(r)}{p_\infty} = \left[\gamma^{-1/(\gamma-1)}\left(6\gamma^2\frac{p_\infty}{\rho_l a_l^2}\right)^{1/(2\gamma-1)}\right]^{-(\gamma-0.38)}\left(\frac{\Delta p}{p_\infty}\right)^{(\gamma-0.38)/(2\gamma-1)}\left(\frac{r}{R_0}\right)^{-1.13}, \tag{9}$$

where γ is the polytropic index and r is the radius of the radially propagating shock wave [16]. We assume that the shock pressure scales in the same way for collapse in a corner. Neglecting bubble migration during collapse and assuming the jet impacts the bubble wall at the centroid, the distance from the bubble to the wall in the direction of travel of the jet and the distance from the bubble to the corner are $L_w = \delta_x/\cos\theta_j$ and $L_c = \sqrt{\delta_x^2+\delta_z^2}$, respectively. The pressures at the wall and corner, given the shock pressure is greatest in line with the jet [16], are then $p_w = 2p_{bc}L_w^{-1.13}$ and $p_c = 4p_{bc}L_c^{-1.13}$, where p_{bc} is the shock pressure immediately after the collapse. The coefficients 2 and 4 come from the image bubbles doubling and quadrupling the shock pressure at the wall and corner, respectively, and the power of -1.13 is based on underwater explosion scalings [42]. The ratio of pressures at the wall and corner is then

$$\frac{p_c}{p_w} = 2\left(\frac{L_c}{L_w}\right)^{-1.13} = 2\left(\frac{\delta_x}{\cos\theta_j\sqrt{\delta_x^2+\delta_z^2}}\right)^{1.13}. \tag{10}$$

All of the constants divide out such that the ratio of pressures depends only on the initial stand-off distances. This result directly predicts the initial stand-off distances for which the maximum pressure occurs directly in the corner. As observed in experiments [22] and in the present simulations, the bubble migrates during its collapse due to the presence of the walls. Given that the shock emitted upon collapse decays as it propagates outward, closer proximity to the wall(s) at the instant of collapse results in higher pressures than if that same shock had been released at the initial centroid location. The degree of motion toward each wall is straightforward to calculate as described in Sec. III C. As such, we replace δ_x and δ_z with $\delta_{xc} = \delta_x - \Delta_{xm}$ and $\delta_{zc} = \delta_z - \Delta_{zm}$ to find

$$p_r = 2\left(\frac{\delta_{xc}}{\cos\theta_j\sqrt{\delta_{xc}^2+\delta_{zc}^2}}\right)^{1.13} \approx 2\left(\frac{\delta_x - a\zeta_x^{3/5} - b}{\cos\theta_j\sqrt{\left(\delta_x - a\zeta_x^{3/5} - b\right)^2 + \left(\delta_z - a\zeta_z^{3/5} - b\right)^2}}\right)^{1.13}. \tag{11}$$

This semiempirical expression predicts the region in δ_x-δ_z space for which the pressure in the corner exceeds that on either wall, taking into consideration the motion of the bubble centroid. The jet angle can be predicted using only the initial stand-off distances with Eq. (6) or (8). Comparing this expression to our simulation results, the wall location δ_{zp} at which the maximum pressure is achieved is shown in Fig. 13. The region of initial stand-off distances where Eq. (11) predicts $p_r \geqslant 1$, i.e., the maximum pressure occurs in the corner, is shown in gray. The maximum pressure is achieved

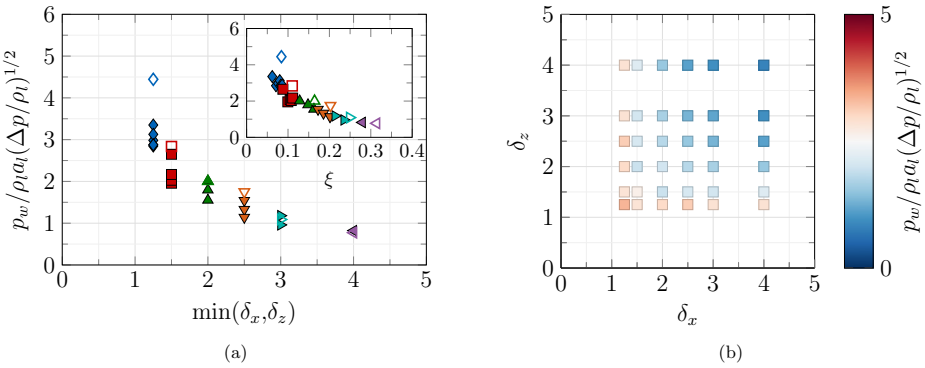

FIG. 14. Maximum wall pressure vs (a) $\min(\delta_x, \delta_z)$ and ξ (inset) and (b) initial stand-off distances. Blue diamonds denote $\delta_x = 1.25$, red squares $\delta_x = 1.5$, green deltas $\delta_x = 2.0$, orange gradients $\delta_x = 2.5$, teal right triangles $\delta_x = 3.0$, and purple left triangles $\delta_x = 4.0$. Corner cases are closed and single-wall cases are open.

in the corner for cases that lie along the $\delta_x = \delta_z$ line due to the double reflection of the shock at that location, as well as for those cases within a certain range of this line. In all other cases, the maximum pressure occurs within $0.5R_o$ from the closest initial wall location, in the direction of the corner, consistent with the jet angle. Overall, the agreement between our simulations and our theoretical model (11) is good, indicating that the location of the maximum wall pressure near a corner is well described using these shock interactions. If the desired effect is to reduce damage in a corner of a component undergoing repeated cavitation, this result suggests that a design that minimizes nucleation sites with $\delta_x/\delta_z \approx 1$ is desirable. Conversely, if high pressure in the corner is desirable (as may be the case for ultrasonic cleaners) then maximizing nucleation sites with $\delta_x/\delta_z \approx 1$ would be optimal.

The maximum wall pressure itself is a key quantity of interest in cavitation damage. Figure 14 shows the maximum wall pressures for different initial stand-off distances. The highest wall pressures occur for collapse closest to the walls, as expected. The maximum wall pressure decreases quickly with initial stand-off distance for collapse both near a corner and near a single wall because of the decay of the emitted shock with propagation distance. When parametrized by ξ, the pressures produced by collapse near a single wall are consistently higher than those produced by collapse near two walls. This follows from (i) the decreased jet speeds for collapse near a corner, which result in a lower water-hammer pressure, and (ii) the larger minimum volumes of collapse near a corner, which result in a weaker implosion shock. These two differences in the dynamics are a direct consequence of the second wall making up the corners. Those cases for which the wall pressures are higher for collapse near a corner than for collapse near a single wall are cases where the reflected shocks intersect at the corner. The difference between the pressures in collapse near a corner and collapse near a single wall decreases with increasing distance from the walls as the effect on the walls becomes small. The asymmetry of the collapse due to the second wall generally manifests in less effective focusing of the energy in the collapse, leading to weaker shocks and therefore lower wall pressures than those produced in collapse near a single wall. It follows that the presence of the second wall is generally expected to decrease the damage potential of bubble collapse compared to collapse near a single wall.

E. Wall temperatures

Certain materials may be sensitive to temperatures produced during the bubble collapse [4], in which case the maximum wall temperature is an important quantity of interest. As illustrated in [16], bubble collapse near a single wall can increase the wall temperature via two mechanisms: (i) As it reflects off the wall, the shock emitted upon collapse raises the temperature of the water

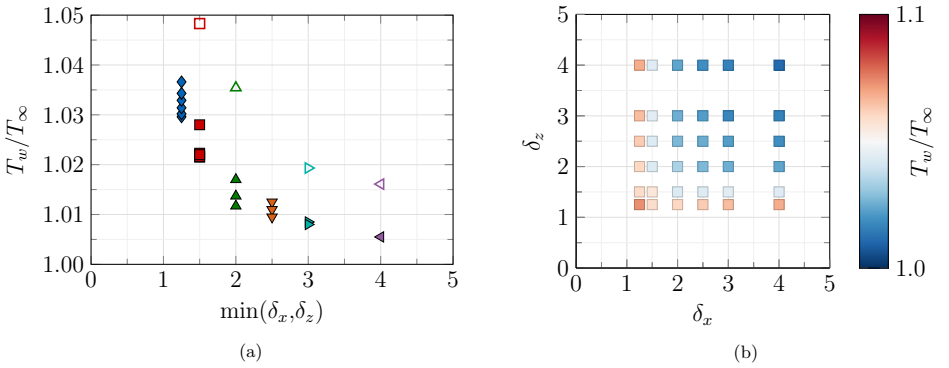

FIG. 15. Maximum wall temperature (UHMWPE) vs (a) $\min(\delta_x, \delta_z)$ and (b) initial stand-off distances. Blue diamonds denote $\delta_x = 1.25$, red squares $\delta_x = 1.5$, green deltas $\delta_x = 2.0$, orange gradients $\delta_x = 2.5$, teal right triangles $\delta_x = 3.0$, and purple left triangles $\delta_x = 4.0$. Corner cases are closed and single-wall cases are open.

adjacent to the wall for a short period, and (ii) bubbles sufficiently close to the wall come into close proximity to the wall at collapse, at which point their contents can reach a high temperature and lead to heat conduction to the wall. The resulting wall temperature can be calculated by solving the corresponding heat conduction problem. Though both mechanisms are short lived, the relatively large temperature difference can give rise to significant changes in wall temperatures. The maximum wall temperature achieved during collapse near a corner is shown in Fig. 15 for different initial stand-off distances assuming properties corresponding to ultrahigh-molecular-weight polyethylene (UHMWPE) as it is relevant to applications of interest [28]. Most cases follow mechanism (i), with the shock wave impingement creating a transient increase in the wall temperature. Bubbles initially closest to one or both walls (i.e., with the smallest ratio δ_x/δ_z) follow mechanism (ii), whereby the bubble comes in contact with the wall. The importance of contact is visible by considering the cases with $\delta_x = 1.25$ and increasing δ_z; the wall temperature increases despite the maximum wall temperature of all cases considered occurring for $\delta_x = \delta_z = 1.25$.

Though not shown here for conciseness, the locations of the maximum wall temperatures exhibit a behavior similar to the locations of the maximum wall pressures. Cases for which δ_x/δ_z is close to unity experience the maximum wall temperature directly in, or very close to, the corner. Other cases give rise to the maximum wall temperature along the wall, away from the corner. Equation (11) can also be used to determine initial stand-off distances for which the maximum wall temperature occurs in the corner rather than along the wall. Initial stand-off distances for which the maximum temperature occurs in the corner exactly match those for which the maximum pressure occurs in the corner.

The temperatures calculated here do not however reach the melting point of the wall and thus significant damage is unlikely caused as a direct result of the heat produced; instead, experimentally observed damage is likely primarily due to increased wall pressure. This finding is consistent with that of Beig *et al.* [16] for UHMWPE. Despite the inability of a single bubble to reach melting temperatures, repeated collapses may transfer sufficient heat to cause damage. Materials with lower melting temperatures may also be susceptible to melting.

IV. ATTACHED BUBBLES

Bubbles attached to a rigid surface have been shown to produce high pressures [1] as the reentrant jet directly impinges upon the surface. Additionally, given the direct contact of the hot gas at minimum volume, high wall temperatures may be produced. Although the contact line dynamics

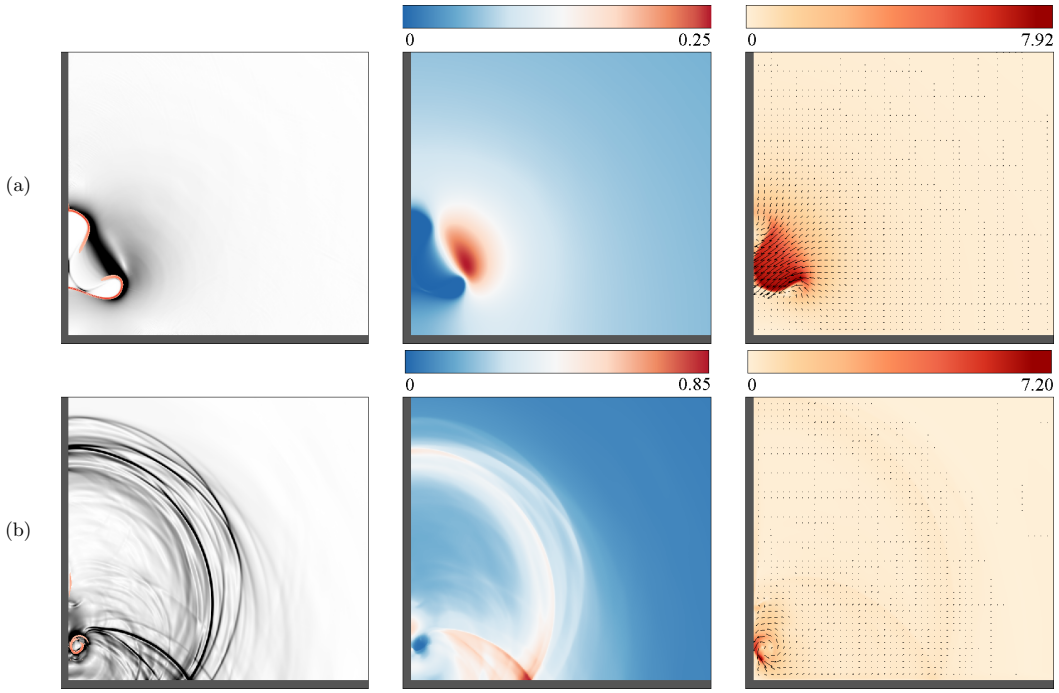

FIG. 16. Contours of (numerical) schlieren, pressure normalized by $\rho_l a_l \sqrt{\Delta p/\rho_l}$ and velocity magnitude normalized by the characteristic interfacial speed $\sqrt{\Delta p/\rho_l}$ for $(\delta_x, \delta_z) = (0.75, 1.25)$ at (a) $t = 1.387$ and (b) $t = 1.607$.

cannot be represented in the present numerical framework, we assume like Trummler *et al.* [27] that their effect is negligible given the present interest in inertia-dominated collapse.

Figures 16 and 17 show contours of numerical schlieren, pressure, and velocity magnitude for simulations with $(\delta_x, \delta_z) = (0.75, 1.25)$ and $(\delta_x, \delta_z) = (0.25, 0.75)$. The bubble is immediately aware of the wall(s) to which it is attached. A reentrant jet develops, again at an angle that is not normal to the attached wall, and penetrates the bubble. The jet directly impinges upon the wall, thereby generating an intricate set of shocks that further interact with the bubble. In the $(\delta_x, \delta_z) = (0.75, 1.25)$ case, the bubble appears to take a toroidal shape with one part attached to the wall, while for $(0.25, 0.75)$ the bubble converges toward the corner and eventually detaches from one side after the shock is generated.

As compared to collapse of a bubble initially detached from the walls, the shock waves produced by collapse of a bubble initially attached to one or both walls are more numerous and complex. This is a consequence of the impact of the reentrant jet on the wall, which reflects the generated shock back into the portions of the bubble attached to the wall. This reflected shock propagates through the bubble and impinges upon the air-water interface of the bubble wall and generates a reflected rarefaction which returns to the wall and further contributes to the number of waves present in the flow field. The direct impact of the reentrant jet on the wall produces high pressures along the wall, and the strength of the shock does not decay significantly as they travel to the walls due to their proximity to the walls. As such, the wall pressures produced by collapse of a bubble initially attached to one or both walls are expected to be higher than those produced by collapse of a bubble initially detached from both walls.

Conversely, the strong effects of the wall are expected to reduce the intensity of collapse for attached bubbles. Figure 18 shows the collapse times for different values of δ_z. The collapse times decrease with increasing δ_z and are slower than in the detached case, as expected due to the more

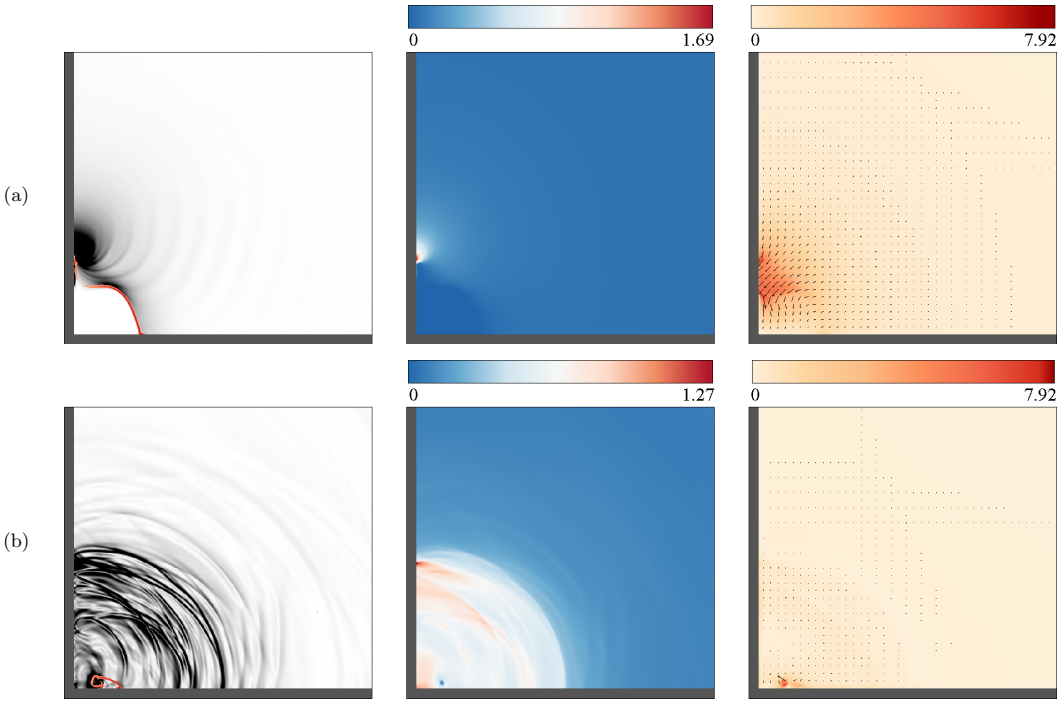

FIG. 17. Contours of (numerical) schlieren, pressure normalized by $\rho_l a_l \sqrt{\Delta p/\rho_l}$ and velocity magnitude normalized by the characteristic interfacial speed $\sqrt{\Delta p/\rho_l}$ for $(\delta_x, \delta_z) = (0.25, 0.75)$ at (a) $t = 1.319$ and (b) $t = 1.493$.

rapid reduction in driving pressure following wave reflection off the wall. The lack of a strong dependence on δ_x indicates that the collapse time depends most on the shock reflecting off the far wall. As previously discussed, a longer collapse time implies a less violent collapse, which is consequential for the jet speed and maximum wall pressure.

The jet angles point almost directly toward the corner for small δ_z and decrease with increasing δ_z. Consistent with the collapse times, the data do not show variability with δ_x; they also approach the expected value of $\theta_j = 0$ as δ_z is increased toward δ_{cr}. The jet angle of bubbles initially attached to one or either wall does not appear to follow (6) or (8), which implies potential flow does not accurately approximate the collapse dynamics, likely due to the significant compressibility effects.

The ambivalence toward δ_x in both the collapse time and jet angle of the attached cases (particularly those attached to only one wall) is likely because the initial rarefaction travels normal to the bubble surface, so the effect of the wall is not experienced by the bubble interface until the radially converging transmitted shock wave reflects off the walls and returns to the bubble interface. The rarefaction returning from the far wall breaks the axisymmetry and nonuniformly changes the driving pressure around the bubble, hence the strong dependence on δ_z.

Consistent with the collapse times, the jet speeds are lowest for collapse closest to the corner. While for each value of δ_x the jet speed does not increase monotonically with increasing distance from the corner, the jet speeds are generally increasing. The maximum jet speed depends on the local dynamics, which is complex due to the wave-interface interactions, such that their dependence on δ_x is not straightforward and we observe this nonmonotonic behavior. As for fully detached bubbles, the jet speeds are lower than in collapse near a single wall. Compared to the jet speeds observed for fully detached bubbles, the jet speeds observed here are generally lower, again suggesting that the collapse of bubbles initially attached to either wall are less violent than their initially detached counterparts.

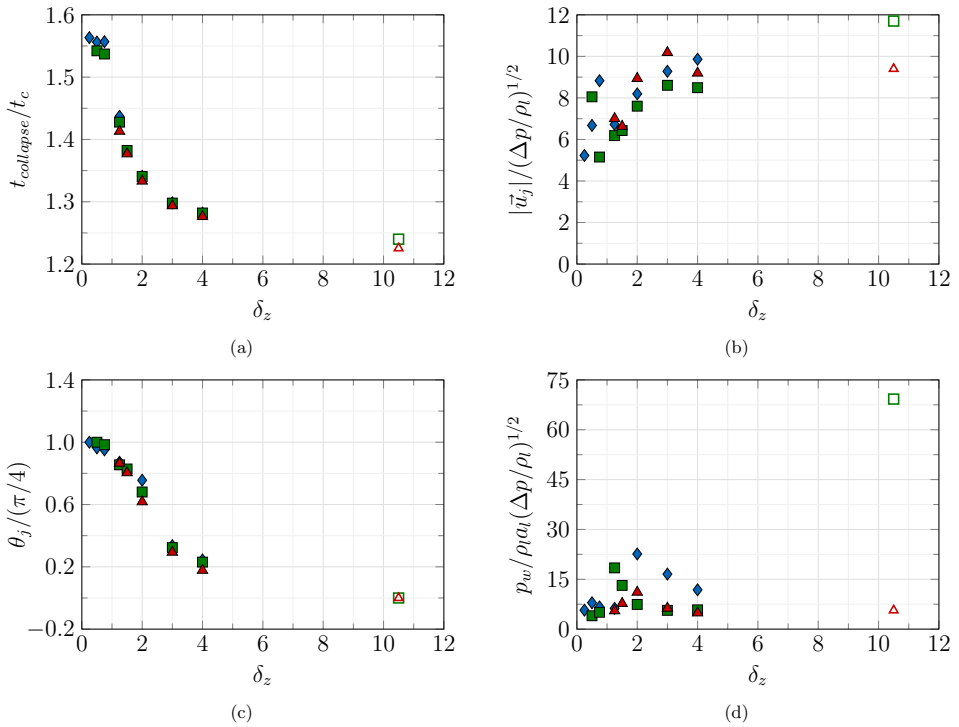

FIG. 18. (a) Collapse time, (b) jet speed, (c) jet angle, and (d) maximum wall pressure vs δ_z. Blue diamonds denote $\delta_x = 0.25$, green squares $\delta_x = 0.5$, and red deltas $\delta_x = 0.75$. Corner cases are closed and single-wall cases are open.

The maximum wall pressure occurs where the jet impinges upon the wall and is thus dependent on the jet angle. The resulting maximum wall pressure depends on two competing factors: On one hand, the jet speeds are lower for attached bubbles than for detached bubbles, so the water-hammer pressure is expected to be lower; on the other hand, the bubble is closer, if not touching the wall, such that the wall experiences the full effect of the jet impact.

There are two regions of behavior for each δ_x value. For $\delta_x = 0.25$ and 0.75, when $\delta_z < 2$ there is no clear trend in the pressure. The same is noted for $\delta_x = 0.5$ and $\delta_z < 1.25$, and similar to the maximum jet speed, in these cases the dynamics are governed by the complex shock-interface interactions and characterization is not straightforward. For $\delta_x = 0.25$ and 0.75, when $2 \leqslant \delta_z \leqslant \delta_c$, and for $\delta_x = 0.5$, when $1.25 \leqslant \delta_z \leqslant \delta_c$, we observe a monotonic decrease in the maximum wall pressure with increasing δ_z. The maximum wall pressure appears to converge to the limiting case of bubble collapse near a single wall for $\delta_x = 0.75$; however, collapse near a single wall with $\delta_x = 0.5$ shows a substantially higher pressure. This behavior results from a faster reentrant jet which causes a strong water hammer. We expect that as δ_z approaches δ_{cr} the maximum wall pressures for $\delta_x = 0.5$ and 0.25 increase to match those in collapse near a single wall.

V. CONCLUSION

In this article we conducted high-resolution numerical simulations of Rayleigh collapse of a gas bubble near a corner for varying initial stand-off distances to understand the role of the second (perpendicular) wall in Rayleigh collapse near a single wall. We were particularly interested in the maximum pressure produced along the wall and the phenomena governing it, as this quantity is the most consequential hydrodynamic metric for cavitation erosion.

Compared to collapse near a single wall, a bubble is affected by the second wall only if it is within a critical distance from the wall based on the time it takes for the initially released rarefaction to reflect back to the bubble. This reflected rarefaction wave alters the pressure distribution around the bubble, thereby modifying the pressure field by reducing it locally and giving rise to an asymmetric distribution. In the case of collapse near a corner, the different parts of the rarefaction interact with the bubble at different times depending on the initial stand-off distance. This reflection off the second wall communicates the presence of the extra image sinks and breaks the axisymmetry of the converging flow, leading to a deflection of the reentrant jet toward the corner. As such, the angle of the jet can be parametrized solely by the ratio of stand-off distances. Other key collapse properties (e.g., collapse time, minimum volume, and maximum jet speed) can also be described by a single parameter, the deviation from spherical shape of the bubble, which can be related to the Kelvin impulse. Overall, the presence of the second wall inhibits the collapse, i.e., collapse times are slower, minimum volumes are larger, and jet speeds are slower when the bubble collapses in a corner compared to collapse near a single wall. These dynamics lead to shock emission with properties different from those observed in collapse near a single wall, in the following ways: (i) The maximum reentrant jet speed (and thus water-hammer shock magnitude) is reduced by the proximity to the second wall, (ii) the highest magnitude along the emitted shock front is in the direction of the jet and thus not in the direction normal to either wall, and (iii) the migration of the bubble toward the closest wall is hindered by the second wall such that the bubble collapses farther from the closest wall than in collapse near a single wall. The combination of these effects leads to, in general, wall pressures that are lower than it would in the case of collapse near a single wall. An additional difference is that the second wall causes an additional reflected shock, which interacts with the shock reflected off the original wall. A consequence is the doubling of pressure in the corner and enhanced wall pressure. Using theoretical arguments, we developed expressions for the maximum wall pressure produced by bubble collapse near a corner and determine which initial stand-off distances lead to higher pressures in the corner than along the closest wall. We also considered heat transfer during this process, as well as the collapse of attached bubbles.

This work sets the stage for studies in more intricate geometries, as well as collapse of a larger number of bubbles. In such situations, bubbles may form along rigid surfaces, such that contact line dynamics may need to be investigated.

ACKNOWLEDGMENTS

This research was performed using funding received from the DOE Office of Nuclear Energy's Nuclear Energy University Programs (Grant No. DE-NE0008747). Simulations were conducted on the Blue Waters sustained petascale computing project, which is supported by the National Science Foundation (Awards No. OCI-0725070 and No. ACI-1238993), the State of Illinois, and as of December, 2019, the National Geospatial-Intelligence Agency. Blue Waters is a joint effort of the University of Illinois at Urbana-Champaign and its National Center for Supercomputing Applications.

[1] Y. Tomita and A. Shima, Mechanisms of impulsive pressure generation and damage pit formation by bubble collapse, J. Fluid Mech. **169**, 535 (1986).

[2] A. Vogel, W. Lauterborn, and R. Timm, Optical and acoustic investigations of the dynamics of laser-produced cavitation bubbles near a solid boundary, J. Fluid Mech. **206**, 299 (1989).

[3] A. Philipp and W. Lauterborn, Cavitation erosion by single laser-produced bubbles, J. Fluid Mech. **361**, 75 (1998).

[4] T. Deplancke, O. Lame, J. Y. Cavaille, M. Fivel, M. Riondet, and J. P. Franc, Outstanding cavitation erosion resistance of ultra high molecular weight polyethylene (UHMWPE) coatings, Wear **328–329**, 301 (2015).

[5] Lord Rayleigh, On the pressure developed in a liquid during the collapse of a spherical cavity, Philos. Mag. **34**, 94 (1917).
[6] C. D. Ohl, O. Lindau, and W. Lauterborn, Luminescence from Spherically and Aspherically Collapsing Laser Induced Bubbles, Phys. Rev. Lett. **80**, 393 (1998).
[7] Y. T. Didenko, W. B. McNamara, and K. S. Suslick, Molecular emission from single-bubble sonoluminescence, Nature (London) **407**, 877 (2000).
[8] M. P. Brenner, S. Hilgenfeldt, and D. Lohse, Single-bubble sonoluminescence, Rev. Mod. Phys. **74**, 425 (2002).
[9] D. J. Flannigan, S. D. Hopkins, C. G. Camara, S. J. Putterman, and K. S. Suslick, Measurement of Pressure and Density Inside a Single Sonoluminescing Bubble, Phys. Rev. Lett. **96**, 204301 (2006).
[10] W. Lauterborn and T. Kurz, Physics of bubble oscillations, Rep. Prog. Phys. **73**, 106501 (2010).
[11] O. Supponen, D. Obreschkow, P. Kobel, M. Tinguely, N. Dorsaz, and M. Farhat, Shock waves from nonspherical cavitation bubbles, Phys. Rev. Fluids **2**, 093601 (2017).
[12] O. Lindau and W. Lauterborn, Cinematographic observation of the collapse and rebound of a laser-produced cavitation bubble near a wall, J. Fluid Mech. **479**, 327 (2003).
[13] C. F. Naudé and A. T. Ellis, On the mechanism of cavitation damage by nonhemispherical cavities collapsing in contact with a solid boundary, J. Basic Eng. **83**, 648 (1961).
[14] T. B. Benjamin and A. T. Ellis, The collapse of cavitation bubbles and the pressure thereby produced against solid boundaries, Philos. Trans. R. Soc. London Ser. A **260**, 221 (1966).
[15] M. S. Plesset and R. B. Chapman, Collapse of an initially spherical vapour cavity in the neighbourhood of a solid boundary, J. Fluid Mech. **47**, 283 (1971).
[16] S. A. Beig, B. Aboulhasanzadeh, and E. Johnsen, Temperatures produced by inertially collapsing bubbles near rigid surfaces, J. Fluid Mech. **852**, 105 (2018).
[17] K. H. Kim, G. Chahine, J. P. Franc, and A. Karimi, Advanced Experimental and Numerical Techniques for Cavitation Erosion Prediction, edited by K.-H. Kim, G. Chahine, J.-P. Franc, and A. Karimi, *Fluid Mechanics and its Applications* (Springer, Dordrecht, 2014), Vol. 106.
[18] E. A. Brujan, G. S. Keen, A. Vogel, and J. R. Blake, The final stage of the collapse of a cavitation bubble close to a rigid boundary, Phys. Fluids **14**, 85 (2002).
[19] W. Lauterborn and H. Bolle, Experimental investigations of cavitation-bubble collapse in the neighbourhood of a solid boundary, J. Fluid Mech. **72**, 391 (1975).
[20] E. Johnsen and T. Colonius, Numerical simulations of non-spherical bubble collapse, J. Fluid Mech. **629**, 231 (2009).
[21] E.-A. Brujan, A.-M. Zhang, Y.-L. Liu, T. Ogasawara, and H. Takahira, Jetting and migration of a laser-induced cavitation bubble in a rectangular channel, J. Fluid Mech. **948**, A6 (2022).
[22] E. A. Brujan, T. Noda, A. Ishigami, T. Ogasawara, and H. Takahira, Dynamics of laser-induced cavitation bubbles near two perpendicular rigid walls, J. Fluid Mech. **841**, 28 (2018).
[23] J. Cui, Z.-P. Chen, Q. Wang, T.-R. Zhou, and C. Corbett, Experimental studies of bubble dynamics inside a corner, Ultrason. Sonochem. **64**, 104951 (2020).
[24] Y. Tagawa and I. R. Peters, Bubble collapse and jet formation in corner geometries, Phys. Rev. Fluids **3**, 081601(R) (2018).
[25] L. Molefe and I. R. Peters, Jet direction in bubble collapse within rectangular and triangular channels, Phys. Rev. E **100**, 063105 (2019).
[26] S.-M. Li, A.-M. Zhang, Q. X. Wang, and S. Zhang, The jet characteristics of bubbles near mixed boundaries, Phys. Fluids **31**, 107105 (2019).
[27] T. Trummler, S. H. Bryngelson, K. Schmidmayer, S. J. Schmidt, T. Colonius, and N. A. Adams, Near-surface dynamics of a gas bubble collapsing above a crevice, J. Fluid Mech. **899**, A16 (2020).
[28] S. A. Beig and E. Johnsen, Maintaining interface equilibrium conditions in compressible multiphase flows using interface capturing, J. Comput. Phys. **302**, 548 (2015).
[29] M. Rodriguez and E. Johnsen, A high-order accurate five-equations compressible multiphase approach for viscoelastic fluids and solids with relaxation and elasticity, J. Comput. Phys. **379**, 70 (2019).
[30] J. P. Franc, M. Riondet, A. Karimi, and G. L. Chahine, Impact load measurements in an erosive cavitating flow, J Fluids Eng. **133**, 121301 (2011).

[31] A. Murrone and H. Guillard, A five equation reduced model for compressible two phase flow problems, J. Comput. Phys. **202**, 664 (2005).
[32] N. A. Hawker and Y. Ventikos, Interaction of a strong shockwave with a gas bubble in a liquid medium: A numerical study, J. Fluid Mech. **701**, 59 (2012).
[33] A. Tiwari, C. Pantano, and J. B. Freund, Growth-and-collapse dynamics of small bubble clusters near a wall, J. Fluid Mech. **775**, 1 (2015).
[34] O. Le Métayer and R. Saurel, The Noble-Abel stiffened-gas equation of state, Phys. Fluids **28**, 046102 (2016).
[35] S. Gottlieb and C. W. Shu, Total variation diminishing Runge-Kutta schemes, Math. Comput. **67**, 73 (1998).
[36] G.-S. Jiang and C.-W. Shu, Efficient Implementation of weighted ENO schemes, J. Comput. Phys. **126**, 202 (1996).
[37] E. Johnsen and T. Colonius, Implementation of WENO schemes in compressible multicomponent flow problems, J. Comput. Phys. **219**, 715 (2006).
[38] M. T. Henry de Frahan, S. Varadan, and E. Johnsen, A new limiting procedure for discontinuous Galerkin methods applied to compressible multiphase flows with shocks and interfaces, J. Comput. Phys. **280**, 489 (2015).
[39] J. B. Keller and M. Miksis, Bubble oscillations of large amplitude, J. Acoust. Soc. Am. **68**, 628 (1980).
[40] O. Supponen, D. Obreschkow, M. Tinguely, P. Kobel, N. Dorsaz, and M. Farhat, Scaling laws for jets of single cavitation bubbles, J. Fluid Mech. **802**, 263 (2016).
[41] V. Streeter, E. Wylie, and K. Bedford, *Fluid Mechanics* (WCB/McGraw Hill, New York, 1998).
[42] R. H. Cole, *Underwater Explosions* (Princeton University Press, Princeton, 1948).